ADVANCED FUNCTIONAL MATERIALS
www.afm-journal.de

Carbon Nanotube Based Inverted Flexible Perovskite Solar Cells with All-Inorganic Charge Contacts

Qiang Luo, He Ma, Feng Hao, Qinzhi Hou, Jing Ren, Lili Wu, Zhibo Yao, Yu Zhou, Ning Wang, Kaili Jiang,* Hong Lin,* and Zhanhu Guo**

Organolead halide perovskite solar cells (PSC) are arising as promising candidates for next-generation renewable energy conversion devices. Currently, inverted PSCs typically employ expensive organic semiconductor as electron transport material and thermally deposited metal as cathode (such as Ag, Au, or Al), which are incompatible with their large-scale production. Moreover, the use of metal cathode also limits the long-term device stability under normal operation conditions. Herein, a novel inverted PSC employs a SnO_2-coated carbon nanotube (SnO_2@CSCNT) film as cathode in both rigid and flexible substrates (substrate/NiO-perovskite/Al_2O_3-perovskite/SnO_2@CSCNT-perovskite). Inverted PSCs with SnO_2@CSCNT cathode exhibit considerable enhancement in photovoltaic performance in comparison with the devices without SnO_2 coating owing to the significantly reduced charge recombination. As a result, a power conversion efficiency of 14.3% can be obtained on rigid substrates while the flexible ones achieve 10.5% efficiency. More importantly, SnO_2@CSCNT-based inverted PSCs exhibit significantly improved stability compared to the standard inverted devices made with silver cathode, retaining over 88% of their original efficiencies after 550 h of full light soaking or thermal stress. The results indicate that SnO_2@CSCNT is a promising cathode material for long-term device operation and pave the way toward realistic commercialization of flexible PSCs.

1. Introduction

In the past few years, metal halide perovskite solar cells (PSCs) attract increasing attention due to their high efficiency, low material and fabrication cost, and scalable manufacture capability.[1–4] Owing to the ambipolar semiconducting characteristics, perovskite materials have been widely investigated in two solar cell configurations, ranging from mesoscopic to planar structures with N-I-P or P-I-N architectures. With continued advances of the perovskite compositions, film growth technologies, charge contacts, and optimization of device interfaces,[5–9] the maximum power conversion efficiency (PCE) of single-junction PSCs has been boosted to a certified 22.1% for small area device[10] and close to 20% for 1 cm^2 size device,[11,12] approaching the efficiency of commercialized crystalline silicon and CIGS solar cells. Although high efficiency has been demonstrated, stability and material cost are two dominant factors that retard the commercialization of PSCs.[13–15]

In most of the state-of-the-art inverted P-I-N PSCs, organic transport layers, such as (6,6)-phenyl-C_{61}-butyric acid methyl ester (PCBM),[16] C_{60} and their derivatives,[17,18] have been commonly used as n-type electron collecting materials. Although incorporating organic semiconductor layers can provide high efficiencies and reduced hysteresis,[19,20] the high price of organic semiconductors could hinder the advantage of the rapid energy payback of perovskites. In addition, the thin

Dr. Q. Luo, Dr. F. Hao, Q. Hou, J. Ren, Prof. N. Wang
State Key Laboratory of Electronic Thin Film and Integrated Devices
University of Electronic Science and Technology of China
Chengdu 610054, P. R. China
E-mail: wangninguestc@gmail.com

Dr. H. Ma
College of Applied Sciences
Beijing University of Technology
Beijing 100124, P. R. China

Dr. H. Ma, Prof. K. Jiang
State Key Laboratory of Low-Dimensional Quantum Physics
Tsinghua-Foxconn Nanotechnology Research Center
Department of Physics
Collaborative Innovation Center of Quantum Matter
Tsinghua University
Beijing 100084, P. R. China
E-mail: JiangKL@mail.tsinghua.edu.cn

Dr. L. Wu, Prof. Z. Guo
Integrated Composites Laboratory (ICL)
Department of Chemical and Biomolecular Engineering
University of Tennessee
Knoxville, TN 37996, USA
E-mail: zguo10@utk.edu

Z. Yao, Y. Zhou, Prof. H. Lin
State Key Laboratory of New Ceramics and Fine Processing
School of Material Science, and Engineering
Tsinghua University
Beijing 100084, P. R. China
E-mail: hong-lin@mail.tsinghua.edu.cn

Prof. N. Wang
State Key Laboratory of Marine Resource Utilization in South China Sea
Hainan University
Haikou 570228, P. R. China

The ORCID identification number(s) for the author(s) of this article can be found under https://doi.org/10.1002/adfm.201703068.

DOI: 10.1002/adfm.201703068

organic buffer layer is also insufficient to effectively protect the perovskite layer from moisture damage in a humid environment. On the other hand, the most frequently used metal back contacts, such as silver and aluminum or even gold, have still been achieved with high-vacuum thermal deposition technologies. The energy requirements associated with high vacuum processing hinder the large-scale production of PSCs.[13] Moreover, the interface deterioration by chemical reaction between metal electrodes and perovskite created a significant performance degradation of PSCs.[21–23] Although organic buffer layers inserted between the metal electrodes and the perovskite layer may to a certain extent relieve the device performance degradation over a short time scale,[24,25] but cannot solve the long-term stability issue because the perovskite and metal electrodes tend to diffuse through the organic buffer layers after long-term operation under illumination or thermal stress.[26–29] For example, Wang and co-workers recently investigated the thermal stability of inverted structured PSCs (FTO/NiO/$CH_3NH_3PbI_3$/PCBM/Ag) using time-of-flight secondary ion mass spectroscopy (ToF-SIMS) and observed the diffusion of methylammonium and iodide ions from CH_3 NH_3 PbI_3 through the PCBM to accumulate at the Ag internal surface.[30] Consequently, the deteriorated $CH_3NH_3PbI_3$ thin film and the generation of AgI barrier resulted in the degradation of device efficiencies. Several studies showed that spatially separating the perovskite layer and metal back electrode could effectively slow down the performance degradation, including replacing organic buffer layer with compact ZnO[31] and inserting an inorganic Nb-doped TiO_x buffer layer between fullerene and metal cathode.[32] However, fundamental solutions to those instability factors still rely on developing low-cost and stable cathodes which are much less reactive with perovskite absorber.

Carbon materials have been proven to be competitive alternative to metals to serve as back electrode in conventional N-I-P PSCs as a result of their high conductivity, chemical stability, and abundance.[33–37] For example, Han and co-workers developed a promising hole-conductor-free mesoscopic PSC using a structure of FTO/TiO_2-perovskite/ZrO_2-perovskite/carbon(graphite)-perovskite,[33,38] in which the perovskite solution was casted into the TiO_2 scaffold from porous carbon/graphite electrode side by a simple drop-infiltration method. The drop-infiltration deposition technology is advantageous for large-scale production of PSCs owing to the low material usage.[33] While the high temperature requirement associated with the carbon/graphite composite electrode (over 450 °C) limits the device fabrication on flexible plastic substrates. In contrast, carbon nanotube (CNT) films can be integrated into devices without any sintering and are especially interesting in electrode material for flexible PSCs due to their high conductivity and flexibility. However, although the use of CNT as back electrodes in normal PSCs has been reported, studies on the exploration of CNT as stable cathodes for inverted PSCs have been quite sparse up to date. Herein we report for the first time, an inverted NiO/$CH_3NH_3PbI_3$ planar PSC with freestanding porous Al_2O_3 nanotube spacer and SnO_2-coated cross-stacked superaligned carbon nanotube (SnO_2@CSCNT) cathode. By coating a layer of electron-extracting SnO_2 on the CSCNT film, perovskite devices with SnO_2@CSCNT electrode show significantly eliminated photocurrent hysteresis and enhanced device performance. Furthermore, flexible PSCs with over 10% efficiency were also achieved by adopting the same inverted architecture as their rigid counterpart. In addition, SnO_2@CSCNT-based PSCs exhibited considerably enhanced device stability compared to the standard inverted devices made with organic electron transport layer and silver cathode, retaining about 88% of their original efficiencies after over 500 h thermal annealing or light soaking.

2. Results and Discussion

Figure 1a illustrates the device architecture of the inverted NiO/$CH_3NH_3PbI_3$ planar PSC with SnO_2@CSCNT as cathode. The p-type NiO hole conductor layer was prepared by atomic layer deposition method. CSCNT in SnO_2@CSCNT hybrid film served as current collector, which was fabricated by stacking the superaligned CNT layers crossly in sequence.[39–41] SnO_2 grown on CSCNT was used as n-type electron conductor, which was prepared by coating tin precursor on the surface of CSCNT film followed by annealing (Figure 1b). The cross-stacking porous

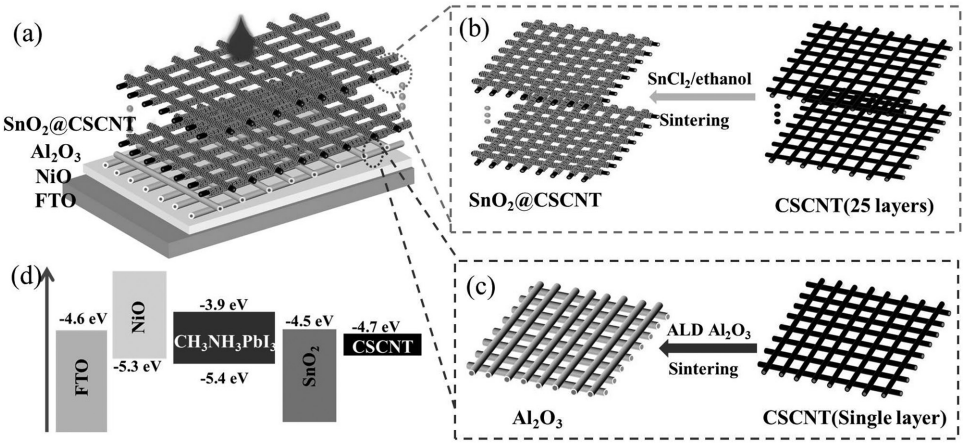

Figure 1. Schematic illustration of a) PSC architecture, preparation process of b) SnO_2@CSCNT hybrid electrode and c) Al_2O_3 nanotube film; d) energy level diagram in PSCs.

Al_2O_3 nanotube film was prepared by coaxially coating Al_2O_3 on the single-layer CSCNT followed by annealing to remove the carbon cores (Figure 1c).[42] Perovskite was incorporated into the devices by solution drop-casting method from SnO_2@CSCNT side. The precursor solution travelled through the SnO_2@CSCNT layer and Al_2O_3 spacer layer and finally reached the NiO hole contact. Figure 1d shows the corresponding energy level diagram of the prepared inverted PSCs. Under light illumination, the perovskite layer ($CH_3NH_3PbI_3$) absorbs photons and generates excited electrons and holes, subsequently the electrons and holes in the $CH_3NH_3PbI_3$ perovskite can be extracted and transfer to the SnO_2 (–4.0 eV) and NiO (–5.2 eV), respectively.

The scanning electron microscope (SEM) images of CSCNT, Al_2O_3, and SnO_2@CSCNT films are shown in **Figure 2**a–c. CSCNT film demonstrates a typical cross-stacking structure (Figure 2a), in which CNTs are generally parallel to each other within the same layer, and perpendicular to each other between neighboring layers.[40,41] The Al_2O_3 film also exhibits cross-stacking and porous features as its CSCNT template (Figure 2b), which will provide enough room for perovskite loading. In the case of SnO_2@CSCNT electrode (Figure 2c), the SnO_2 nanoparticles are continuous and uniform coating on the surface of CSCNT. The favorable SnO_2 coating can be ascribed to the cross-stacking structure and surface defect of the CSCNT. First, the cross-stacking structure of CSCNT film will facilitate the diffusion of SnO_2 precursors throughout the film. Furthermore, the surfaces of CSCNT are rich in defects such as broken sp_2 bonds,[35] which are expected to provide sufficient active nucleation sites for the SnO_2 growth.[43] The conductivity of the CSCNT and SnO_2@CSCNT films was also evaluated. The hybrid SnO_2@CSCNT film has a sheet resistance (51 ± 2.3 Ω □$^{-1}$), which is similar to that of the original CSCNT sheet (44 ± 1.7 Ω □$^{-1}$). This result indicates that the cross-stacking joints between neighboring CSCNT layers retain good contact even after SnO_2 coating. The reason for this is that the CSCNT framework has been constructed before the SnO_2 coating is formed. This is in contrast to the case where SnO_2 is first coated on individual CNT and then a CSCNT network is formed. In the latter case, the CNT in SnO_2@CSCNT film is isolated by the poorly conductive SnO_2 between CNT junctions, the conductivity and mechanical flexibility are thus largely suppressed. Figure 2d displays the X-ray diffraction (XRD) patterns of the CSCNT and SnO_2@CSCNT films. The peaks at 26.6°, 33.9°, and 51.8° can be assigned to the (110), (101), and (211) faces of the rutile crystalline phase of SnO_2 (JCPDS No. 01-077-0447), respectively.[44] Figure S1 (Supporting Information) compares the Raman spectra of the CSCNT and SnO_2@CSCNT films. The SnO_2@CSCNT film shows the D and G bands from CSCNT and typical tetragonal SnO_2 Raman modes.[45]

The cross-sectional SEM image of a complete solar cell fabricated with a SnO_2@CSCNT cathode is shown in **Figure 3**a. The total thickness of the device is about 4 µm, consisting of a 500 nm FTO conductive layer, a 1.4 µm thick perovskite filled Al_2O_3 spacer layer, and a 2.2 µm thick perovskite filled SnO_2@CSCNT layer. The surface SEM image of perovskite grown in the Al_2O_3 spacer layer is shown in Figure S2 (Supporting Information). It was found that the perovskite formed within the porous Al_2O_3 matrix exhibited large crystal size while it was difficult to quantify the grain size distribution because of the irregular perovskite crystals. The perovskite quality was

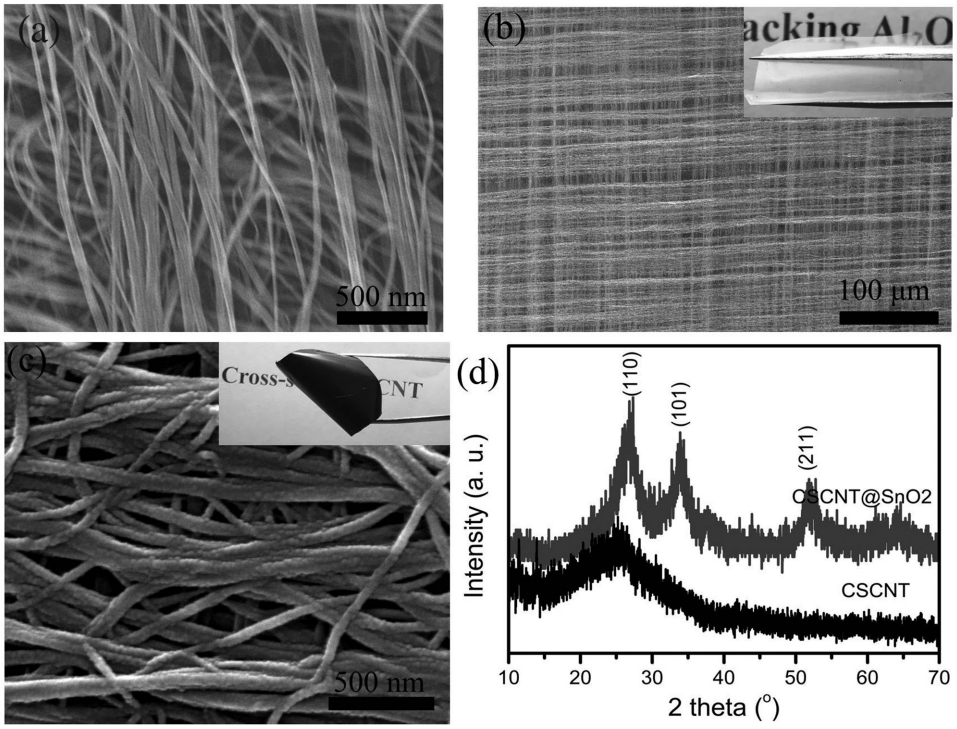

Figure 2. Typical SEM images of a) CSCNT film, b) Al_2O_3 nanotube film, and c) SnO_2@CSCNT film. d) XRD pattern of the CSCNT and SnO_2@CSCNT films. Insets in (b) and (c) are the photo images of freestanding Al_2O_3 and SnO_2@CSCNT films.

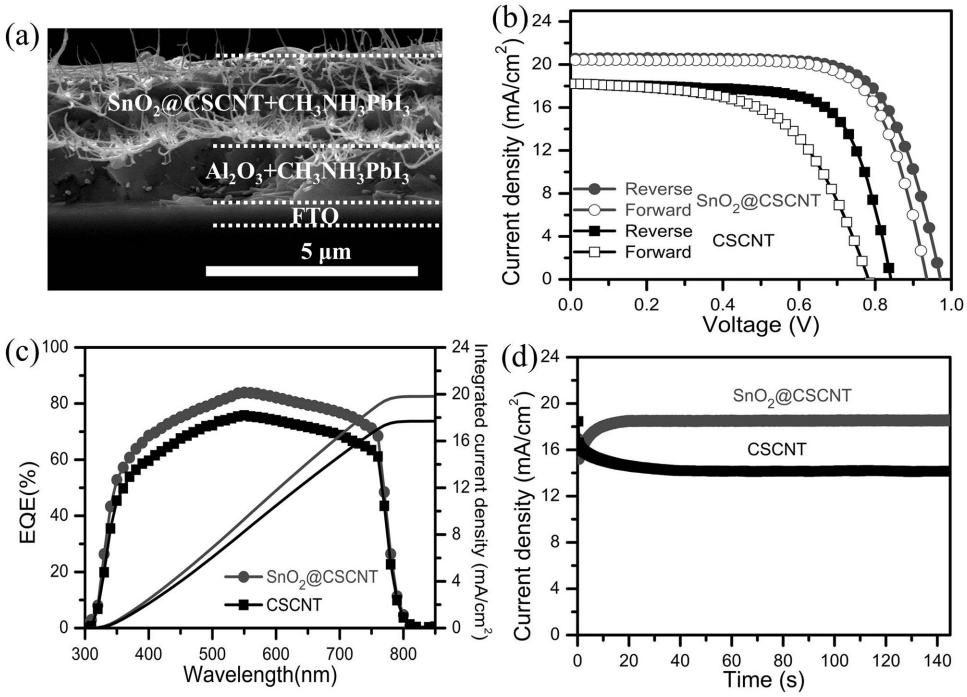

Figure 3. PSC structure and device performances with SnO_2@CSCNT cathode. a) Cross-sectional SEM images of the SnO_2@CSCNT-based PSCs, b) *J–V* curves of PSCs with CSCNT and SnO_2@CSCNT cathodes, c) EQE spectra of CSCNT and SnO_2@CSCNT devices, and d) the photocurrent density as a function of time for the cells held at a forward bias of the maximum output power points (0.67 and 0.76 V for the CSCNT and SnO_2@CSCNT devices, respectively).

further studied by collecting the time-resolved photoluminescence (TRPL) spectra. As shown in Figure S3 (Supporting Information), the carrier lifetime was estimated to ≈70.1 ns, comparable with that of the pure perovskite film (72.1 ns) prepared by conventional spin-costing method. Figure 3b shows the photocurrent density–voltage (*J–V*) characteristics of the champion devices using different electrodes (CSCNT and SnO_2@CSCNT) under AM 1.5G irradiation (100 mW cm^{-2}). The corresponding device parameters including short-circuit current density (J_{sc}), open-circuit voltage (V_{oc}), and fill factor (FF) are summarized in Table S1 (Supporting Information). The control device fabricated with CSCNT electrode exhibited a PCE of 10.7%, with V_{oc} of 0.84 V, J_{sc} of 18.2 mA cm^{-2}, and FF of 0.70 under the reverse scan (from V_{oc} to J_{sc} scan, scan rate 0.022 V s^{-1}), while the corresponding PCE obtained under the forward scan (from J_{sc} to V_{oc} scan) is 8.2%, showing a severe hysteresis in the *J–V* measurement. Very encouragingly, after coating a layer of SnO_2 electron extraction material on CSCNT, the device shows increased V_{oc} and J_{sc}, leading to appreciably improved PCEs of 14.3 and 13.7% measured under reverse and forward scans, respectively. Figure S4 (Supporting Information) shows the device performance distribution for 14 devices fabricated on different substrates. The PCE variation of devices fabricated on the same substrate was ±0.1–0.3% (four devices fabricated on each substrate). The average J_{sc}, V_{oc}, and FF of the SnO_2@CSCNT-based PSCs are much higher than those of the CSCNT-based devices, yielding ≈35% higher PCE (12.7%) than that of the CSCNT device. In addition, the photovoltaic performances of the CSCNT and SnO_2@CSCNT-based PSCs without the use of Al_2O_3 spacer layers were also investigated. It was found that the SnO_2@CSCNT-based solar cells without Al_2O_3 layers obtained quite low PCEs (<0.02%, Figure S5, Supporting Information), while the CSCNT-based devices did not show efficiency output owing to the short circuit of the devices. The porous Al_2O_3 films play two critical roles in the as-fabricated CSCNT-based devices: (1) providing enough room for perovskite loading to ensure sufficient light absorption and (2) avoiding direct contact between the highly conductive CSCNT or SnO_2@CSCNT and NiO hole extraction layer to prevent the device short circuit. The charge recombination behaviors of the CSCNT and SnO_2@CSCNT-based PSCs fabricated with Al_2O_3 spacer layers were investigated by impedance spectroscopy. Figure S6 (Supporting Information) displays the Nyquist plots of typical devices measured at a forward bias of 0.7 V under AM 1.5G illumination, in which two distinct arcs are observed. The first arc at high-frequency region is usually related to the charge transfer process at the interface, while the second arc in lower-frequency region is attributed to the overall recombination resistance (R_{rec}) in the devices.[46,47] The R_{rec} of the devices can be extracted by fitting the Nyquist plots using the applied equivalent circuit (inset of Figure S6, Supporting Information). The SnO_2@CSCNT-based solar cell shows a higher R_{rec} value (1.39 kΩ) compared to that of CSCNT-based device (0.40 kΩ), indicating a lower recombination rate in the SnO_2@CSCNT-based device. Considering that the back contact is the only different part in these cells, the increased photovoltaic performance and decreased R_{rec} can be attributed to the improved charge extraction at the perovskite/SnO_2@CSCNT interfaces because of SnO_2 is a promising electron transport material for perovskite.[48,49] Figure 3c shows the external quantum

efficiency (EQE) of the CSCNT-based PSCs with and without SnO_2 coating. The integrated J_{sc} from the EQE spectra of the CSCNT-based PSCs is as high as 17.6 mA cm^{-2}, and is further improved to 19.8 mA cm^{-2} with SnO_2 coating. These values are consistent (less than 6% deviation) with the measured J_{sc} from the scanned *J–V* curves, thus confirming the validity of the device performance. Figure 3d presents the stabilized photocurrent outputs of CSCNT and SnO_2@CSCNT-based PSCs measured under a constant bias voltage of 0.67 and 0.76 V (close to the maximum power point), respectively. The photocurrents were ≈14.2 and 18.5 mA cm^{-2}, yielding a stabilized efficiency of 9.5 and 14% for CSCNT and SnO_2@CSCNT-based PSCs, respectively.

With freestanding and flexible features of Al_2O_3 and SnO_2@CSCNT films, flexible PSCs on indium tin oxide/polyethylene naphthalate (ITO/PEN) substrates were fabricated as well, adopting the same configuration as its rigid counterpart with all-inorganic charge extraction materials. **Figure 4**a shows the *J–V* curves of the best-performing flexible PSC fabricated with SnO_2@CSCNT electrode. The champion flexible device delivered a V_{oc}, J_{sc}, and FF of 19.2 mA cm^{-2}, 0.91 V, and 0.60, respectively, leading to a promising PCE of 10.5% under reverse scanning direction. The black square spot indicates the maximum power point obtained from the steady-state measurement, where a highly stable PCE of 10.1% can be obtained. These results clearly demonstrate promising merits of the SnO_2@CSCNT as efficient cathode for flexible PSCs. To the best of our knowledge, this PCE is the highest value reported for flexible CNT-based PSCs (Table S2, Supporting Information).[50,51] Figure 4b presents the EQE spectrum and integral current density of the flexible device as a function of wavelength. The integral current density over the full spectrum was calculated to be 18 mA cm^{-2}. The solar cell efficiency histogram of the flexible PSCs is illustrated in Figure 4c. It unravels an average PCE of 9 ± 0.9% over 30 devices and 70% of the fabricated devices can yield a PCE of >9%. The mechanical durability of the flexible device was also evaluated by repeatedly bending the devices (1.5 cm × 2.5 cm) to a bending radius of 0.4 cm. The dependence of the device photovoltaic parameters on bending cycles is presented in Figure 4d. After 300 bending cycles, the V_{oc} was reduced from 0.9 to 0.86 V. The J_{sc} and FF were mostly affected, the J_{sc} was significantly reduced from 18.2 to 16.5 mA cm^{-2} and the FF was decreased from 0.63 to 0.57. All these decreased the device efficiency from initial 10.3 to 8.2% after 300 bending cycles. The decrease of PCE could be the combined result of the increased series resistance of ITO/PEN substrate, the micro-sized crack formation in perovskite layer, as well as the delamination generated at the interfaces between different layers of flexible devices after continuous bending.[52,53]

When it comes to practical commercial viability, long-term stability of PSCs becomes as important as efficiency. The stabilities of the as-fabricated PSCs in this study were studied under various conditions, including humidity, temperature, and light illumination. For comparison, standard NiO-based inverted PSCs were also fabricated with the device configuration of FTO(ITO/PEN)/NiO/$CH_3NH_3PbI_3$/PCBM/Ag (rigid PCE = 16%, flexible PCE = 14.4%). The humidity stability of the rigid and flexible PSCs was first examined as a function of storage time under a controlled relative humidity of 80% in dark. As shown in **Figure 5**a, both rigid and flexible SnO_2@CSCNT-based PSCs can remain over 80% of their initial PCEs after 600 h storage, significantly outperforming the

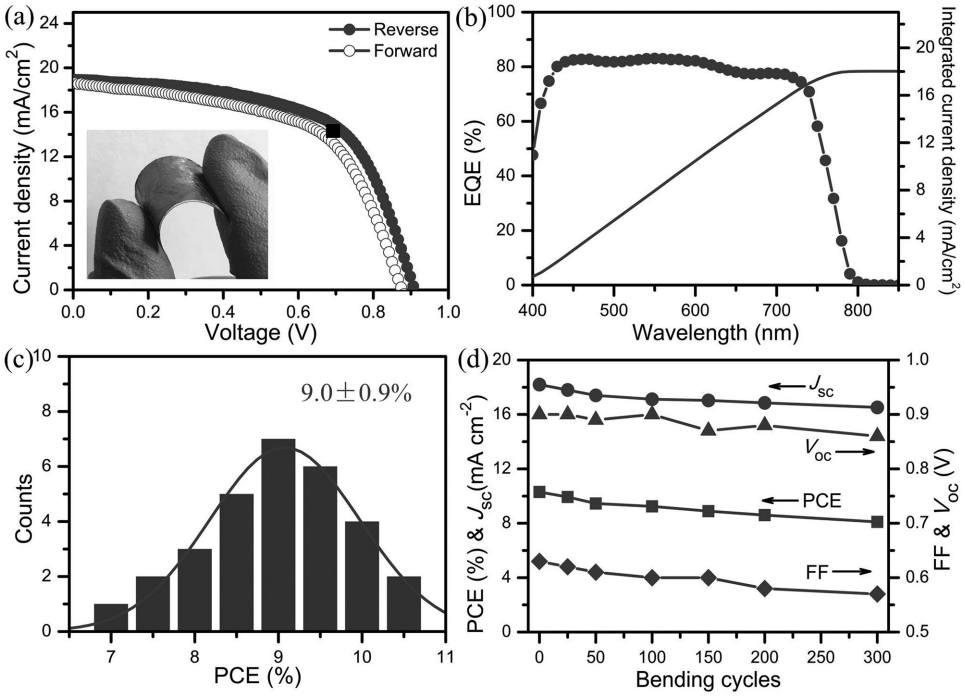

Figure 4. Photovoltaic performance of flexible PSCs with SnO_2@CSCNT cathode. a) *J–V* curves, b) EQE spectra, c) PCE statistics of the flexible devices with SnO_2@CSCNT cathode, the device number for PCE statistics is 30, and d) plot of photovoltaic parameters of flexible device as a function of bending cycles. Inset in (a) is the photograph of a SnO_2@CSCNT-based flexible PSCs.

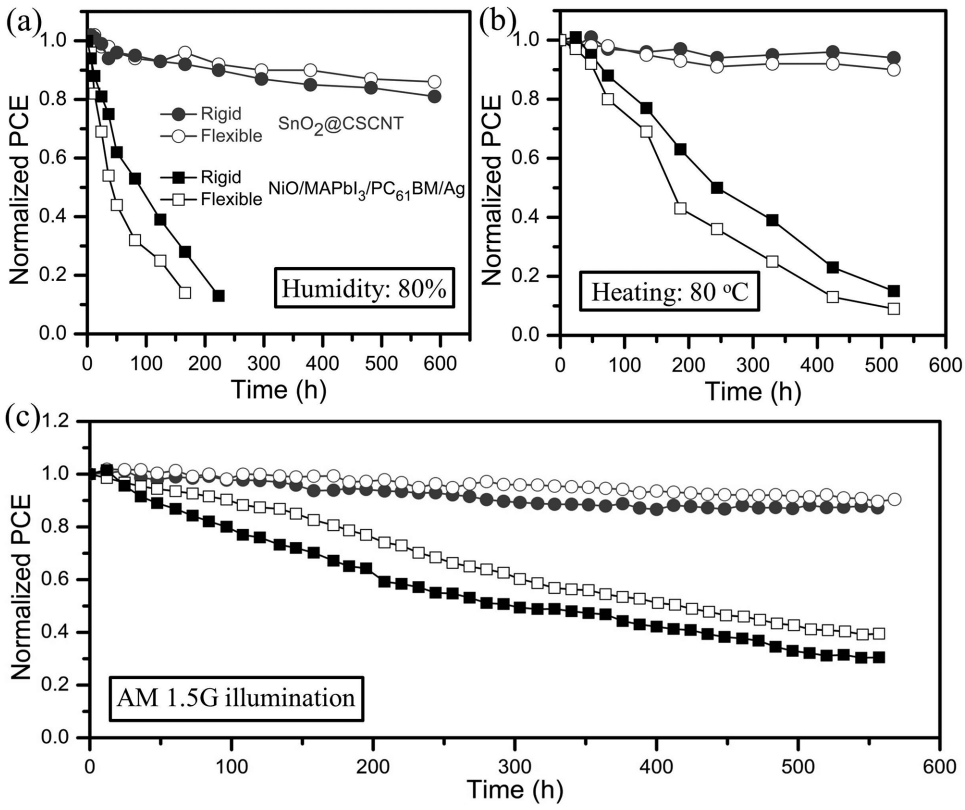

Figure 5. Efficiency stability of standard and SnO_2@CSCNT-based PSCs as a function of soaking time in different environment: a) in ambient atmosphere with a constant relative humidity of 80%, b) in N_2 atmosphere with constant heating temperature of 80 °C, and c) in N_2 atmosphere under AM 1.5G illumination without UV filter.

PCBM-Ag-based standard reference devices. The top surfaces of the devices before and after humidity soaking were examined, as shown in Figure S7 (Supporting Information). It was found that a layer of perovskite with good crystalline quality was formed on the top surface of the fresh devices. After stored in 80% relative humidity in dark after 600 h, the large perovskite crystals decomposed into small PbI_2 nanoparticles. The dense PbI_2 layer that formed at the top of the devices provided an enhanced protection from moisture ingress. In addition, the hydrophobic property of the as-fabricated SnO_2@CSCNT film was also investigated, as shown in Figure S8 (Supporting Information). The contact angle measurement of water droplet on the SnO_2@CSCNT surface showed a contact angle of 85 ± 2.6°, indicating a hydrophobic surface of SnO_2@CSCNT. Moreover, the thick SnO_2@CSCNT-perovskite layer (2.2 µm) also formed a stable encapsulating layer to inhibit further humidity aggression. Therefore, the dense PbI_2 layer, the relatively hydrophobic surface of SnO_2@CSCNT, as well as the thick SnO_2@CSCNT-perovskite layer synergically inhibited the moisture ingress, leading to the enhanced humidity stability of SnO_2@CSCNT-based solar cells. The thermal stability of PSCs was also evaluated in an N_2 glovebox without light illumination. When subjected to a continuous thermal treatment at 80 °C, the reference devices exhibited relatively fast performance degradation, preserving only 20% of their initial values after 530 h (Figure 5b). In sharp contrast, the PCE of rigid SnO_2@CSCNT-based PSCs remained above 90% of its initial value after 530 h, similar to that of flexible devices fabricated on ITO/PEN substrate, suggesting the robustness of SnO_2@CSCNT-based PSCs. In addition, the long-term stability of PSCs was further investigated under AM 1.5G illumination (devices were tested in N_2 atmosphere). As shown in Figure 5c, the efficiency of rigid PSCs preserved 89% of their original values after continuous light illumination for 550 h while the flexible devices retained 91% from their initial values under similar conditions, both show much enhanced stability compared to that of the reference PSCs (≈40%). The above results on device stabilities show that the SnO_2@CSCNT is a promising option for cathode in inverted PSCs.

3. Conclusion

In summary, CSCNT films coated with SnO_2 electron extracting material were first reported to serve as an efficient and non-metal cathode in the application of inverted $CH_3NH_3PbI_3$/NiO PSCs. Compared to the devices fabricated with regular CSCNT films, the charge recombination of SnO_2@CSCNT-based PSCs was significantly reduced by coating SnO_2 electron extracting layer. As a result, the derived CSCNT@SnO_2-based PSCs obtained a high PCE of over 14%. Benefitting from the foldable processability of Al_2O_3 spacer and SnO_2@CSCNT, the flexible devices can be fabricated and exhibit an impressive PCE of 10.5%. Furthermore, both rigid and flexible PSCs demonstrated

good performance preservation under high humidity, thermal stress, or continuous AM 1.5G light soaking. The simple fabrication process and long-term stability of such kind of carbon nanotubes-based inverted $NiO/CH_3NH_3PbI_3$ PSCs open up new avenues for future development of high efficiency and large-scale photovoltaic cells.

4. Experimental Section

Materials: All chemicals were purchased from Sigma-Aldrich and used as received without any purification. Methylammonium iodide (CH_3NH_3I) was synthesized using a previously reported method.[5] To prepare the perovskite precursor, CH_3NH_3I was first dissolved into dimethyl sulfoxide/*N,N*-dimethyl formamide (3:7, volume ratio) and stirred for 2 h. PbI_2 was subsequently added to the CH_3NH_3I solution (PbI_2:CH_3NH_3I, 1:1 molar ratio). The total mass concentration of the perovskite precursor was 33 wt%. Before use, the perovskite precursor solution was filtered through PTFE filters (0.45 µm).

Fabrication of CSCNT, SnO_2@CSCNT, and Al_2O_3: The superaligned CNT arrays comprising CNTs with a length of 300 µm were first synthesized on 6 in. silicon wafers with iron as the catalyst and acetylene as the precursor in a low-pressure chemical vapor deposition (LP-CVD) system.[39] Flowing argon gas was used as the carrier gas, and acetylene served as the carbon source. Prior to growth, the SiO_2/Si wafers were coated with thin Fe films (3.5–5.5 nm) deposited by electron beam evaporation at a low deposition rate of about 0.1 Å s^{-1}. For the growth of superaligned CNT arrays, the substrate was first placed horizontally in the middle of the tube furnaces and then was heated up to the growth temperature of 680–720 °C in the flowing argon gas for 15 min. Then hydrogen and acetylene were injected to the carrier gas. Uniform superaligned arrays with a length of 300 µm on a 6 in. wafer can be achieved under the conditions of 500 sccm acetylene plus 50 sccm hydrogen. The superaligned CNT films can be directly drawn out from the arrays. A CSCNTs film was fabricated by sequentially stacking the superaligned CNTs on a metallic frame along one direction, followed by stacking in its perpendicular direction.[40,41] After that, the CSCNT films were shrunk and tightened by dipping them into ethanol for 30 s. The thickness of CSCNT film was about 2.5 µm. SnO_2@CSCNT was prepared by dropping ethanol solution of $SnCl_2$ (0.001 mol $SnCl_2{\cdot}2H_2O$ and 0.5 mL benzyl alcohol in 5 mL ethanol) on CSCNT films following by sintering the films at 300 °C. Ethanol was selected as the solvent because of its good solubility for $SnCl_2$ and its good wettability with CSCNT. The final loading of SnO_2 on CSCNT was 18% in weight.

Al_2O_3 films were prepared by atomic layer deposition (ALD) method.[42] Amorphous carbon layer (≈2 nm) was first deposited on single-layer CSCNT film in a magnetron sputtering system with a background vacuum of 2.5×10^{-3} Pa. Subsequently, Al_2O_3 was coated on CSCNT in a commercial ALD system (SVTA, NorthStar) under the temperature of 120 °C. Trimethylaluminium, H_2O, and N_2 were used as the aluminum source, oxygen source, and carrier gas, respectively. One ALD cycle contained 0.02 s exposure to trimethylaluminium, 25 s pumping, 0.01 s exposure to H_2O, and 50 s pumping. The flow rate of N_2 was maintained at 5 sccm. Al_2O_3-coated CSCNT was prepared by 210 cycles. Freestanding Al_2O_3 film was obtained after the carbon cores being removed from Al_2O_3-coated CSCNT by annealing in air at 650 °C for 1 h. The diameter of Al_2O_3 nanotube was about 80 nm. The thickness of Al_2O_3 film was about 1.4 µm.

Preparation of NiO Hole Transport Layer: NiO hole collecting layer was prepared on FTO or ITO/PEN substrates by ALD method. Prior to deposition, the substrates were pretreated via UV–ozone for 30 min. $Ni(dmamb)_2$ (dmamb, 1-dimethylamino-2-methyl-2-butanolate) precursor was used as nickel source, O_3 with 15 wt% in O_2 was used as oxidizer. One ALD cycle contained 0.05 s exposure to $Ni(dmamb)_2$, 20 s pumping, 20 s Ar purging, 0.05 s exposure to O_3, 40 s pumping, and 20 s Ar purging. The flow rate of the oxidizer gas was 20 sccm. The reaction system was maintained at 120 °C and the pressure was 3×10^{-3} Pa. The NiO film was finished with 100 ALD cycles and the thickness of NiO was ≈18 nm.

Solar Cell Fabrication: After NiO was deposited on conductive substrates, Al_2O_3 spacer was transferred onto the NiO layer. Subsequently, CSCNT or SnO_2@CSCNT cathode was transferred onto Al_2O_3 spacer layer with the aid of a small droplet of chlorobenzene. 100 µL perovskite precursor was dropped on the top of the cathodes. Then the substrates were spin-coated at 2000 rpm for 60 s, followed by drying at 110 °C on a hot plate for 100 min.

Characterization: The XRD patterns of the as-prepared samples were obtained on a Bruker D8 Advance diffractometer with Cu Kα1 radiation. The morphology of samples was characterized with SEM (LEO 1530, Gemini, Zeiss, Germany). Raman spectra were carried out on a laser micro-Raman spectroscope (Hr800, Horiba Jobin Yvon, France) with a laser beam wavelength of 633 nm. The TRPL decay spectra were collected by using a fluorescence spectrometer instrument (FLS920, Edinburgh Instruments, Livingston, UK). A picosecond pulsed diode laser with excitation wavelength of 405 nm was used to record the emission decay curves.

The current–voltage (*J–V*) curves of the PSCs were recorded by utilizing a digital source meter (2401, Keithley Instruments, USA) under AM 1.5G irradiation (100 mW cm^{-2}), which was realized by a solar simulator (91192, Oriel, USA) and calibrated by a standard silicon solar cell before measurements. The EQE was recorded by using a solar cell quantum efficiency measurement system (QEX10, PV measurements, USA). Impedance spectroscopy measurements were performed by using the Zahner system (Zahner, Zahner-Electrik GmbH&Co. KG, Germany) in the frequency range of 2 MHz to 1 Hz with an amplitude of 5 mV and the Z-view software was used to analyze the impedance data. Impedance spectra were recorded under AM 1.5G illumination. The humidity of the stability measurements was controlled by using a temperature humidity chamber (RP-80A, Beijing Hongzhan Instrument Co., Ltd.). The thermal stability of the solar cells was evaluated by heating the devices at 80 °C in N_2 glovebox. Solar cells were removed from the heating plane and cooled to room temperature before measuring the device efficiencies. The photostability of the devices was performed in N_2 atmosphere under AM 1.5G irradiation.

Supporting Information

Supporting Information is available from the Wiley Online Library or from the author.

Acknowledgements

This work was supported by the China-Japan International Cooperation Program Funds (Nos. 2010DFA61410 and 2011DFA50530), the Joint NSFC-ISF Research Fund (2015DFG52690), National Natural Science Foundations of China (Nos. 51272037, 51272126, 51303116, and 51472043), and Program for New Century Excellent Talents in University (No. NCET-12-0097).

Conflict of Interest

The authors declare no conflict of interest.

Keywords

carbon nanotubes, charge extracting materials, perovskite solar cells, stabilities

Received: June 7, 2017
Revised: July 15, 2017
Published online: September 8, 2017

[1] A. Kojima, K. Teshima, Y. Shirai, T. Miyasaka, *J. Am. Chem. Soc.* **2009**, *131*, 6050.
[2] H. S. Kim, C. R. Lee, J. H. Im, K. B. Lee, T. Moehl, A. Marchioro, S. J. Moon, R. Humphry-Baker, J. H. Yum, J. E. Moser, M. Grätzel, N. G. Park, *Sci. Rep.* **2012**, *2*, 591.
[3] M. M. Lee, J. Teuscher, T. Miyasaka, T. N. Murakami, H. J. Snaith, *Science* **2012**, *338*, 643.
[4] J. Burschka, N. Pellet, S. J. Moon, R. Humphry-Baker, P. Gao, M. K. Nazeeruddin, M. Gratzel, *Nature* **2013**, *499*, 316.
[5] N. J. Jeon, J. H. Noh, W. S. Yang, Y. C. Kim, S. Ryu, J. Seo, S. I. Seok, *Nature* **2015**, *517*, 476.
[6] W. Nie, H. Tsai, R. Asadpour, J. C. Blancon, A. J. Neukirch, G. Gupta, J. J. Crochet, M. Chhowalla, S. Tretiak, M. A. Alam, H. Wang, A. D. Mohite, *Science* **2015**, *347*, 522.
[7] W. S. Yang, J. H. Noh, N. J. Jeon, Y. C. Kim, S. Ryu, J. Seo, S. I. Seok, *Science* **2015**, *348*, 1234.
[8] M. Saliba, T. Matsui, K. Domanski, J. Y. Seo, A. Ummadisingu, S. M. Zakeeruddin, J. P. Correa-Baena, W. R. Tress, A. Abate, A. Hagfeldt, M. Grätzel, *Science* **2016**, *354*, 206.
[9] S. S Shin, E. J. Yeom, W. S. Yang, S. Hur, M. G. Kim, J. Im, J. Seo, J. H. Noh, S. I. Seok, *Science* **2017**, *356*, 167.
[10] National Renewable Energy Laboratory, Best Research-Cell Efficiencies Chart, www.nrelgov/ncpv/images/efficiency_chartjpg (accessed: July 2017).
[11] H. Tan, A. Jain, O. Voznyy, X. Lan, F. P. García de Arquer, J. Z. Fan, R. Quintero-Bermudez, M. Yuan, B. Zhang, Y. Zhao, F. Fan, P. Li, L. N. Quan, Y. Zhao, Z. Lu, Z. Yang, S. Hoogland, E. H. Sargent, *Science* **2017**, *355*, 722.
[12] X. Li, D. Bi, C. Yi, J. D. Décoppet, J. Luo, S. M. Zakeeruddin, A. Hagfeldt, M. Grätzel, *Science* **2016**, *353*, 58.
[13] J. Gong, S. B. Darling, F. You, *Energy Environ. Sci.* **2015**, *8*, 1953.
[14] Y. Yuan, J. Huang, *Acc. Chem. Res.* **2016**, *49*, 286.
[15] S. Wang, Y. Jiang, E. J. Juarez-Perez, L. K. Ono, Y. Qi, *Nat. Commun.* **2016**, *2*, 16195.
[16] Z. Xiao, C. Bi, Y. Shao, Q. Dong, Q. Wang, Y. Yuan, C. Wang, Y. Gao, J. Huang, *Energy Environ. Sci.* **2014**, *7*, 2619.
[17] J. Y. Jeng, Y. F. Chiang, M. H. Lee, S.-R. Peng, T. Guo, P. Chen, T. C. Wen, *Adv. Mater.* **2013**, *25*, 3727.
[18] P. Liang, C. Y. Liao, C. C. Chueh, F. Zuo, S. T. Williams, X. Xin, J. Lin, A. K. Y. Jen, *Adv. Mater.* **2014**, *26*, 3748.
[19] Y. Shao, Z. Xiao, C. Bi, Y. Yuan, J. Huang, *Nat. Commun.* **2014**, *5*, 5784.
[20] Y. Bai, Q. Dong, Y. Shao, Y. Deng, Q. Wang, L. Shen, D. Wang, W. Wei, J. Huang, *Nat. Commun.* **2016**, *7*, 12806.
[21] Y. Han, S. Meyer, Y. Dkhissi, K. Weber, J. M. Pringle, U. Bach, L. Spiccia, Y. Cheng, *J. Mater. Chem. A* **2015**, *3*, 8139.
[22] A. Guerrero, J. You, C. Aranda, Y. S. Kang, G. Garcia-Belmonte, H. Zhou, J. Bisquert, Y. Yang, *ACS Nano* **2016**, *10*, 218.
[23] Y. Kato, L. K. Ono, M. V. Lee, S. Wang, S. R. Raga, Y. Qi, *Adv. Mater. Interfaces* **2015**, *2*, 1500195.
[24] M. Kaltenbrunner, G. Adam, E. D. Glowacki, M. Drack, R. Schwodiauer, L. Leonat, D. H. Apaydin, H. Groiss, M. C. Scharber, M. S. White, N. S. Sariciftci, S. Bauer, *Nat. Mater.* **2015**, *14*, 1032.
[25] W. Chen, Y. Wu, J. Liu, C. Qin, X. Yang, A. Islam, Y. Cheng, L. Han, *Energy Environ. Sci.* **2015**, *8*, 629.
[26] M. Bag, L. A. Renna, R. Y. Adhikari, S. Karak, F. Liu, P. M. Lahti, T. P. Russell, M. T. Tuominen, D. Venkataraman, *J. Am. Chem. Soc.* **2015**, *137*, 13130.
[27] G. Divitini, S. Cacovich, F. Matteocci, L. Cina, C. Ducati, *Nat. Energy* **2015**, *1*, 15012.
[28] K. Domanski, J. Correa-Baena, N. Mine, M. K. Nazeeruddin, A. Abate, M. Saliba, W. Tress, A. Hagfeldt, M. Gratzel, *ACS Nano* **2016**, *10*, 6306.
[29] S. Cacovich, L. Cina, F. Matteocci, G. Divitini, P. A. Midgley, A. D. Carlo, C. Ducati, *Nanoscale* **2017**, *9*, 4700.
[30] J. Li, Q. Dong, N. Li, L. Wang, *Adv. Energy Mater.* **2017**, *7*, 1602922.
[31] J. You, L. Meng, T. Song, T. Guo, Y. Yang, W. Chang, Z. Hong, H. Chen, H. Zhou, Q. Chen, Y. Liu, N. De Marco, Y. Yang, *Nat. Nanotechnol.* **2016**, *11*, 75.
[32] W. Chen, Y. Wu, Y. Yue, J. Liu, W. Zhang, X. Yang, H. Chen, E. Bi, I. Ashraful, M. Grätzel, L. Han, *Science* **2015**, *350*, 944.
[33] A. Mei, X. Li, L. Liu, Z. Ku, T. Liu, Y. Rong, M. Xu, M. Hu, J. Chen, Y. Yang, M. Grätzel, H. Han, *Science* **2014**, *345*, 295.
[34] Z. Wei, K. Yan, H. Chen, Y. Yi, T. Zhang, X. Long, J. Li, L. Zhang, J. Wang, S. Yang, *Energy Environ. Sci.* **2014**, *7*, 3326.
[35] Q. Luo, H. Ma, Y. Zhang, X. Yin, Z. Yao, N. Wang, J. Li, S. Fan, K. Jiang, H. Lin, *J. Mater. Chem. A* **2016**, *4*, 5569.
[36] P. You, Z. Liu, Q. Tai, S. Liu, F. Yan, *Adv. Mater.* **2015**, *27*, 3632.
[37] H. Chen, S. Yang, *Adv. Mater.* **2017**, *24*, 1603994.
[38] Z. Ku, Y. Rong, M. Xu, T. Liu, H. Han, *Sci. Rep.* **2013**, *3*, 3132.
[39] X. Zhang, K. Jiang, C. Feng, P. Liu, L. Zhang, J. Kong, T. Zhang, Q. Li, S. Fan, *Adv. Mater.* **2006**, *18*, 1505.
[40] L. Zhang, C. Feng, Z. Chen, L. Liu, K. Jiang, Q. Li, S. Fan, *Nano Lett.* **2008**, *8*, 2564.
[41] K. Liu, Y. Sun, P. Liu, X. Lin, S. Fan, K. Jiang, *Adv. Funct. Mater.* **2011**, *21*, 2721.
[42] H. Ma, Y. Wei, J. Wang, X. Lin, W. Wu, Y. Wu, L. Zhang, P. Liu, J. Wang, Q. Li, S. Fan, K. Jiang, *Nano Res.* **2015**, *8*, 2024.
[43] J. Di, Z. Yong, Z. Yao, X. Liu, X. Shen, B. Sun, Z. Zhao, H. He, Q. Li, *Small* **2013**, *9*, 148.
[44] J. Song, E. Zheng, J. Bian, X. Wang, W. Tian, Y. Sanehira, T. Miyasaka, *J. Mater. Chem. A* **2015**, *3*, 10837.
[45] Q. Zhao, D. Ju, X. Deng, J. Huang, B. Cao, X. Xu, *Sci. Rep.* **2015**, *5*, 7874.
[46] J. W. Jung, C. C. Chueh, A. K. Y. Jen, *Adv. Mater.* **2015**, *27*, 7874.
[47] X. Yin, P. Chen, M. Que, Y. Xing, W. Que, C. Niu, J. Shao, *ACS Nano* **2016**, *10*, 3630.
[48] E. H. Anaraki, A. Kermanpur, L. Steier, K. Domanski, T. Matsui, W. Tress, M. Saliba, A. Abate, M. Gratzel, A. Hagfeldt, J. P. Correa-Baena, *Energy Environ. Sci.* **2016**, *9*, 3128.
[49] B. Roose, J. P. C. Baena, K. C. Gödel, M. Graetzel, A. Hagfeldt, U. Steiner, A. Abate, *Nano Energy* **2016**, *30*, 517.
[50] I. Jeon, T. Chiba, C. Delacou, Y. Guo, A. Kaskela, O. Reynaud, E. I. Kauppinen, S. Maruyama, Y. Matsuo, *Nano Lett.* **2015**, *15*, 6665.
[51] L. Qiu, J. Deng, X. Lu, Z. Yang, H. Peng, *Angew. Chem. Int. Ed.* **2014**, *53*, 10425.
[52] F. Di Giacomo, A. Fakharuddin, R. Jose, T. M. Brown, *Energy Environ. Sci.* **2016**, *9*, 3007.
[53] Y. Li, L. Meng, Y. Yang, G. Xu, Z. Hong, Q. Chen, J. You, G. Li, Y. Yang, Y. Li, *Nat. Commun.* **2016**, *7*, 10214.

